PCCP

PAPER

View Article Online
View Journal | View Issue

Cite this: *Phys. Chem. Chem. Phys.*, 2017, **19**, 7617

Chiral segregation driven by a dynamical response of the adsorption footprint to the local adsorption environment: bitartrate on Cu(110)†

G. R. Darling,* M. Forster, C. Lin, N. Liu, R. Raval* and A. Hodgson*

Received 27th January 2017,
Accepted 21st February 2017

DOI: 10.1039/c7cp00622e

rsc.li/pccp

Local or global ordering of chiral molecules at a surface is a key step in both chiral separation and heterogeneous enantioselective catalysis. Using density functional theory and scanning probe microscopy results, we find that the accepted structural model for the well known bitartrate on Cu(110) chiral system cannot account for the chiral segregation observed. Instead, we show that this strongly bound, chiral adsorbate changes its adsorption footprint in response to the local environment. The flexible adsorption geometry allows bitartrate to form stable homochiral trimer chains in which the central molecule restructures from a rectangular to an oblique footprint, breaking its internal hydrogen bonds in order to form strong intermolecular hydrogen bonds to neighbouring adsorbates. Racemic structures containing mixed enantiomers do not form strong hydrogen bonds, providing the thermodynamic driving force for the chiral separation that is observed experimentally. This result shows the importance of considering the dynamical response of molecular adsorption footprints at the surface in directing chiral assembly and segregation. The ability of strongly-chemisorbed enantiomers to change footprint depending on the local adsorption environment indicates that supramolecular assemblies at surfaces may exhibit more complex dynamical behaviour than hitherto suspected, which, ultimately, could be tailored to lead to environment and stimuli-responsive chiral surfaces.

1. Introduction

The nanoscale control of chiral molecular assembly at surfaces is of central importance in fields as diverse as chiral separations,[1,2] heterogeneous enantioselective catalysis,[3,4] plasmonics,[5] chiroptical switching[6,7] and biosensors.[8] In all cases, the surface function is profoundly influenced by how individual enantiomers organize at the local and the global level, therefore the outstanding problem in the field is to understand the factors that drive enantiomer assembly and segregation. The importance of intermolecular interactions, such as hydrogen-bonding, steric repulsions and van der Waals interactions, in controlling chiral assembly in 2- and 3-D has been well established.[1,9–15] Recent work has shown that the adsorption footprints adopted by individual molecules also play a critical role in determining the local and global organization of the adsorbed molecules.[16,17] For example, in racemic systems that contain an equal population of right- and left-handed molecules, adsorption footprints are key in determining whether the system organizes into an ordered heterochiral array, spontaneously segregates to form distinct homochiral domains, or assembles as a solid solution with a random arrangement of enantiomers,[18,19] with each arrangement expected to elicit very different physical, chemical and biological responses.

The assembly of enantiopure bitartrate on Cu(110) represents the first global homochiral surface reported in the literature and has become a model system, serving as a benchmark for understanding chiral phenomena in 2D systems.[20–29] Here, we show that the widely-accepted model for this structure,[20–24] based on a rectangular adsorption footprint for bitartrate, is unable to explain either the chiral segregation that is observed for racemic adsorption, or the contrast observed in scanning tunnelling microscopy (STM) images. Using dispersion corrected density functional theory (DFT) we show that the global ordering and chiral segregation arises from the ability of bitartrate to change its adsorption footprint in response to the local environment. Bitartrate forms trimers in which the central bitartrate molecule over-rides the adsorption preference of an individual molecule and locally re-structures to adopt an oblique footprint. In doing so, this bitartrate breaks its internal hydrogen bonds and instead forms hydrogen bonds to the carboxylate groups of the two neighbouring bitartrate units. This local dynamical response by 1/3 of the molecules in the trimer leads to the formation of

Surface Science Research Centre and Department of Chemistry, University of Liverpool, Liverpool L69 3BX, UK. E-mail: darling@liverpool.ac.uk, raval@liverpool.ac.uk, ahodgson@liverpool.ac.uk

† Electronic supplementary information (ESI) available. See DOI: 10.1039/c7cp00622e

strong inter-molecular hydrogen bonds that stabilise the homochiral structure, providing the driving force for chiral segregation.

The molecular adsorption footprint is of central importance in dictating the supramolecular assembly of molecules at surfaces and the orientation of their functional groups, which in turn dictate the response of the interface to the environment, to guest molecules and the alignment of reactants in 'modifier-directed' heterogeneous enantioselective catalysis.[4,30,31] The 'chiral footprint model' is also implicated in the origin of optical activity in metal-based electronic transitions.[7,32] Our work shows the importance of considering the dynamical response of the molecular adsorption footprint to the local adsorption environment, leading to more nuanced behaviour than hitherto anticipated, which could, ultimately, be tailored to create environment and stimuli-responsive chiral surfaces.

2. Methods

STM images were recorded in an ultra high vacuum STM (Specs 150 Aarhus at 100 K or Createc STM/AFM at 77 K) operated in constant current mode with an electrochemically etched tungsten tip. Images were acquired in constant current mode, with bias voltages quoted relative to the sample, so that positive voltages correspond to electrons tunnelling into the surface (empty state images). The copper surface was prepared by argon ion sputtering at 500 eV, followed by annealing to 800 K, yielding an average terrace size of approx. 800 Å. Further details have been given previously.[33] Tartaric acid (99%) was obtained from Sigma Aldrich and used without further purification. The adsorbate was deposited from a small resistively heated glass tube, separated from the main vacuum chamber by a gate valve and differentially pumped by a turbomolecular pump.[20,34] The sample was thoroughly outgassed at *ca.* 340 K and then heated to *ca.* 370 K to sublime on to the copper crystal. During sublimation the chamber pressure was typically $<2 \times 10^{-9}$ mbar. Following deposition the sample was heated to 350 K to order the bitartrate phase.

Total energy calculations were carried out for trial structures using VASP[35,36] with the optB86b-vdW exchange–correlation functional,[37,38] which includes dispersion interactions. We note that previous calculations examined bitartrate adsorption and lateral interactions in smaller unit cells,[22,23] and total energy calculations including dispersion forces have not been reported for the correct chiral unit cell. Single molecule adsorption was modelled with a (5×4) supercell in a 5 layer slab, with the bottom two layers fixed, using a $7 \times 6 \times 1$ *k*-point mesh, while the (1 2, −9 0) (*R*,*R*) unit cell used a $12 \times 4 \times 1$ *k*-point set. Valence electron–core interactions were included using the projector augmented wave method,[39,40] a plane wave cutoff energy of 400 eV and including dipole corrections perpendicular to the surface. All adsorption energies are quoted in eV per molecule, calculated relative to tartaric acid and hydrogen in the gas phase. STM images were calculated using the Tersoff–Hamann approximation in the implementation by Lorente and Persson.[41,42]

3. Results

3.1 STM of bitartrate on Cu(110)

Adsorption of tartaric acid on Cu(110) has become a model system for exploring chiral assembly at surfaces. Tartaric acid has two chiral centres (designated either *R* or *S*), and two carboxylic acid groups that are directly involved in bonding to the surface. The system displays a number of different phases as the acid successively dehydrogenates to form the monotartrate and then bitartrate species.[20,21,24,43–46] The doubly dehydrogenated bitartrate phase, formed by adsorbing tartaric acid above 350 K, undergoes classic Pasteur resolution, with a racemic mixture of (*R*,*R*) and (*S*,*S*) tartaric acid spontaneously segregating into separate mirror domains of the pure enantiomers to form locally organised homochiral domains,[20,21] Fig. 1. Enantiopure adsorption leads to a globally organised homochiral assembly, where a single-handed organisation is sustained from the nano- to the macro-scale.

Fig. 1a shows the STM image of racemic tartaric acid adsorbed on Cu(110), forming segregated domains of (*R*,*R*) (1 2, −9 0) and (*S*,*S*) (9 0, −1 2) structure, respectively. Fig. 1b shows an STM image for the *R*,*R* bitartrate structure in greater detail. The bitartrate adopts a unique single-handed chiral organisation, containing extended chiral chains running along the [1 −1 4] direction, assembled from trimers aligned in a staggered arrangement across the close packed Cu rows. A well-defined gap is found between the bitartrate chains. The STM images are rather insensitive to the bias voltage, although the contrast of the channel is sensitive to the tip state (see ESI† for more detail). Current models of the bitartrate phase[22–24] are based on bitartrate bonding to the surface *via* both

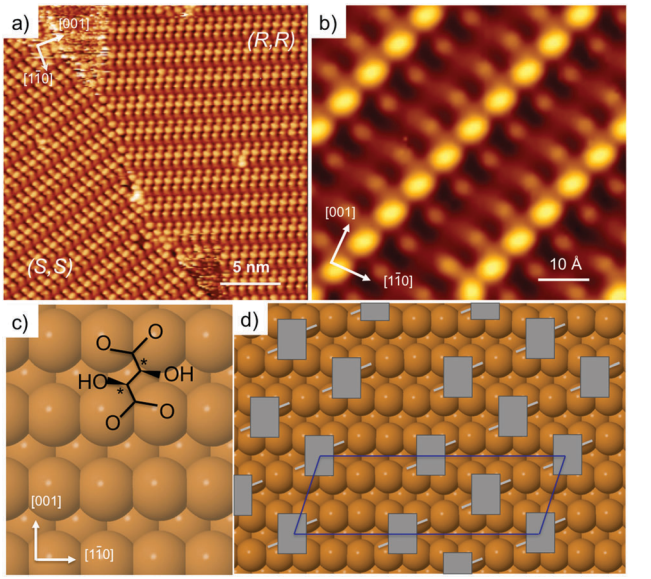

Fig. 1 STM images showing (a) domains of (9 0, −1 2) (*S*,*S*) and (1 2, −9 0) (*R*,*R*) bitartrate formed by dosing a racemic mixture of tartaric acid (300 K, −880 meV, 500 pA) and (b) a high resolution image of the (*R*,*R*) structure formed by dosing a single enantiomer (77 K, −510 meV, 280 pA). Schematics showing (c) the (*R*,*R*) bitartrate molecule (chiral centres marked *) and (d) the arrangement of (*R*,*R*) bitartrate in the (9 0, −1 2) unit cell proposed previously.[22]

carboxylate groups, bridging across adjacent close packed Cu rows to create a rectangular (R_{ec}) footprint, as shown in Fig. 1c. Although it was originally suggested that the bitartrate trimers were linked by hydrogen bonds,[20] subsequent DFT calculations concluded that the bitartrate molecules retain their intra-molecular hydrogen bonds and do not participate in direct inter-molecular interactions, with the chiral arrangement attributed to an improved packing energy for homochiral (*R*,*R*) bitartrate in the structure shown in Fig. 1d.[22] However, the STM data for these homochiral domains, Fig. 1b, show that the central feature of each bitartrate trimer images considerably brighter than the outer units. Under some tip conditions the central feature of the bitartrate structure splits, (probably caused by bitartrate or another adsorbate on the tip, see ESI†), again, imaging quite differently from the outer units. The inequivalence of the central feature in STM is surprising; if the structure is built from three non-interacting bitartrate units, each adsorbed with a rectangular footprint and equivalent at the local level,[22] it is not clear why the central feature should image so differently from its neighbours.

3.2 Theoretical modelling

To understand the structure of bitartrate on Cu(110) we carried out total energy calculations using VASP[35,36] with the optB86b-vdW exchange–correlation functional,[37,38] which includes dispersion interactions. We note that previous calculations examined bitartrate adsorption and lateral interactions in smaller unit cells,[22,23] without including dispersion forces, and total energy calculations have not been reported for the correct chiral unit cell.

i. Adsorption of the isolated molecule. The adsorption of isolated bitartrate on Cu(110) was first investigated. In accord with previous work,[22,23] bitartrate is found to adsorb bridging across two Cu close packed rows, with each carboxylate group adsorbed in the short bridge geometry, bonded to the surface by four Cu–O bonds. Fig. 2 shows the adsorption structure for three different configurations, having either a rectangular footprint (R_{ec}) or with the carboxylate O atoms displaced ±1 unit along ⟨1−10⟩ to give oblique footprints (O_a or O_b). In the rectangular arrangement bitartrate is able to form internal hydrogen bonds between the α-hydroxyls and O of the adjacent carboxylate ligand, creating a strained 5 member ring with a strong hydrogen bond (d_{H-O} = 2.00 Å). Formation of the internal hydrogen bond displaces the α-carbon towards the hydrogen bonded O ligand, distorting the C–C chain away from the ⟨001⟩ direction to give a C–C torsion angle of −28°. Accommodation into the O_a oblique footprint increases the bitartrate torsion angle (ϕ = −50°) and causes the internal hydrogen bond to break, but a new 'trans'-hydrogen bond (d_{H-O} = 2.10 Å) forms between the hydroxyl and O of the opposite carboxylate ligand. The resulting structure is just 0.083 eV less stable than for the rectangular footprint. This oblique footprint is analogous to that found for bisuccinate, which does not have an internal hydrogen bond to satisfy, where calculations find the O_a arrangement is 0.045 eV more stable than the R_{ec} footprint.[47] Choosing the other O_b oblique footprint twists the carbon skeleton back the other way (ϕ = +41°). The internal hydrogen bond between hydroxyl and the adjacent carboxylate ligand is retained, but distortion of the C skeleton stretches (d_{H-O} = 2.86 Å) and weakens the bonds such that the O_b structure is 0.42 eV less stable than the rectangular R_{ec} footprint, (Table S1, ESI†). Although the rectangular footprint is the most stable, the R_{ec} and O_a structures are sufficiently close in energy to suggest that both arrangements are viable candidate structures that may participate in an extended 2D bitartrate phase. This freedom to adopt different footprints without incurring a large energy penalty introduces flexibility in the local response of individual molecules to their environment, a point that becomes important in directing the supramolecular assembly, as discussed below.

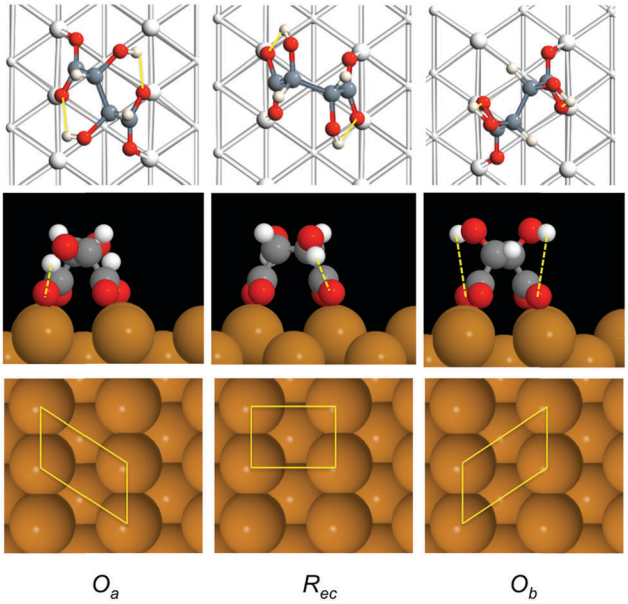

Fig. 2 Calculated structures for (*R*,*R*) bitartrate adsorbed in different sites on Cu(110) in the O_a, R_{ec} and O_b geometries. The top row shows the twisting of the carbon chain (dark grey atoms) and the location of the O ligands (red atoms) relative to the surface Cu atoms. Internal hydrogen bonds are indicated by the yellow lines. The footprint of the Cu atoms involved in bonding to bitartrate in the 3 different geometries is shown schematically in the bottom panel.

ii. Modelling the global assembly. To investigate the global assembly of bitartrate into chiral domains we looked at the stability of different (*R*,*R*), (*S*,*S*) and mixed (*R*,*R*)/(*S*,*S*) bitartrate structures in the (1 2, −9 0) unit cell found experimentally for (*R*,*R*) bitartrate. In view of the poor stability of the O_b arrangement, we focused on structures built from different stacking combinations of the R_{ec} and O_a structures, with a total of 15 different arrangements considered (see Table 1 and ESI†). Fig. 3a shows the structure (I) originally proposed for this phase and the two most stable structures found in this study (Fig. 3b and c). In the original structure (I), the bitartrate trimer has a $R_{ec}R_{ec}R_{ec}$ footprint, with each bitartrate adsorbed next to its neighbour along ⟨1−10⟩ and displaced by 1 unit along ⟨001⟩. The configuration of individual molecules within the trimer is almost identical to that of the isolated R_{ec} monomer, retaining their internal hydrogen bonds, with the binding energy increasing by just 0.013 eV per molecule compared to the monomer. Changing the footprint of the central bitartrate, or the two outer molecules,

Table 1 Binding energy (E_{ad}) of (*R*,*R*), (*S*,*S*) and mixed bitartrate structures in the (1 2, −9 0) unit cell adopted by (*R*,*R*) bitartrate. Each trimer has adjacent bitartrate units offset successively by one unit along ⟨001⟩, as shown in Fig. 3. E_{ad} is the average adsorption energy of bitartrate and ΔE_{ad} the adsorption energy relative to structure II. Further details of structures IV–X are given in the ESI

	Isomers	Footprint	E_{ad} (eV)	ΔE_{ad} (eV)
I	(*R*,*R*):(*R*,*R*):(*R*,*R*)	$R_{ec}R_{ec}R_{ec}$	−2.152	+0.123
II	(*R*,*R*):(*R*,*R*):(*R*,*R*)	$R_{ec}O_aR_{ec}$	−2.275	0.0
III	(*R*,*R*):(*R*,*R*):(*R*,*R*)	$O_aR_{ec}O_a$	−2.244	+0.031
IV	(*R*,*R*):(*R*,*R*):(*R*,*R*)	$O_aO_aO_a$	−2.079	+0.196
V	(*S*,*S*):(*S*,*S*):(*S*,*S*)	$R_{ec}R_{ec}R_{ec}$	−2.163	+0.112
VI	(*S*,*S*):(*S*,*S*):(*S*,*S*)	$R_{ec}O_aR_{ec}$	−2.115	+0.160
VII	(*S*,*S*):(*S*,*S*):(*S*,*S*)	$O_aR_{ec}O_a$	−2.081	+0.194
VIII	(*R*,*R*):(*S*,*S*):(*R*,*R*)	$R_{ec}R_{ec}R_{ec}$	−2.161	+0.114
IX	(*R*,*R*):(*S*,*S*):(*R*,*R*)	$O_aO_aO_a$	−2.157	+0.118
X	(*S*,*S*):(*R*,*R*):(*S*,*S*)	$R_{ec}O_aR_{ec}$	−2.165	+0.110

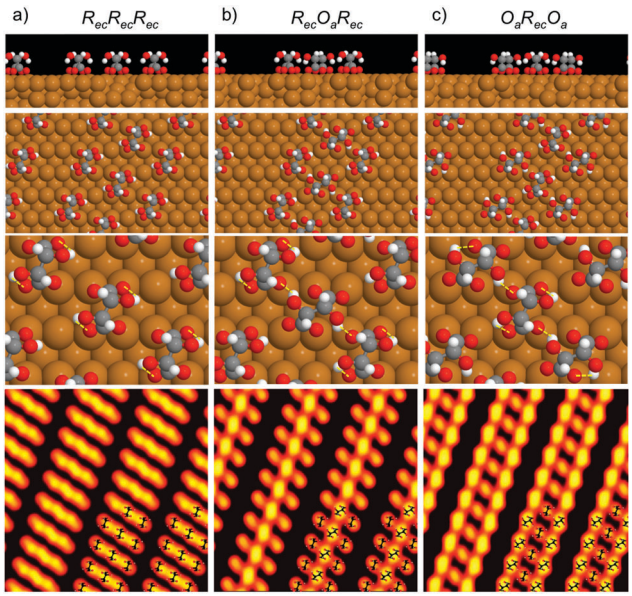

Fig. 3 Calculated structures for (*R*,*R*) bitartrate trimers in the (1 2, −9 0) unit cell, arranged with (a) the $R_{ec}R_{ec}R_{ec}$ configuration, (b) an $R_{ec}O_aR_{ec}$ arrangement and (c) an $O_aR_{ec}O_a$ footprint. The top 2 rows show the end view of the chains and the overall arrangement of bitartrate trimers in the chains. The lower 2 rows show the inter- or intra-molecular hydrogen bonds within a trimer (marked as yellow lines) and, bottom row, simulated STM images for the different structures at the same bias voltage as Fig. 1b, (V = −500 meV).

to an O_a structure allows inter-molecular hydrogen bonds to form, linking the bitartrate row. Fig. 3b shows the $R_{ec}O_aR_{ec}$ arrangement, structure (II), with bitartrate again sitting next to its neighbour along ⟨1−10⟩ and displaced successively by one unit along the ⟨001⟩ direction. In this structure the central O_a unit rearranges, breaking the internal 'trans'-hydrogen bond to form two new hydrogen bonds to the carboxylate groups of the neighbouring R_{ec} bitartrates. With a bond length d_{H-O} = 1.98 Å, the new intermolecular hydrogen bonds are shorter than the internal hydrogen bonds formed by the isolated monomer and the resulting structure is 0.123 eV per molecule more stable than the $R_{ec}R_{ec}R_{ec}$ arrangement. This conclusion is not caused simply by the inclusion of dispersion interactions, since the $R_{ec}O_aR_{ec}$ arrangement remains the more stable structure even when dispersion interactions are neglected entirely using PBE. Intermolecular hydrogen bonds can also be formed by arranging bitartrate in an $O_aR_{ec}O_a$ arrangement, structure (III), shown in Fig. 3c. In this case the intermolecular hydrogen bond length is 2.00 Å, but formation of these bonds causes the internal hydrogen bonds of both the O_a and R_{ec} units to stretch and weaken compared to the ideal monomer geometries. As a result, although the $O_aR_{ec}O_a$ structure is more stable than the $R_{ec}R_{ec}R_{ec}$ arrangement originally proposed, it is slightly (0.032 eV per molecule) less stable than the $R_{ec}O_aR_{ec}$ structure. In fact, our DFT calculations find that the $R_{ec}R_{ec}R_{ec}$ arrangement originally proposed, structure (I), is not even the most stable arrangement for this footprint; stacking $R_{ec}R_{ec}R_{ec}$ trimers directly along the ⟨1−10⟩ close packed direction gives a stronger dispersion interaction and is preferred (see ESI† for further details).

Since the DFT calculations show a clear preference for the bitartrate structure being assembled from $R_{ec}O_aR_{ec}$ trimer units, rather than the $R_{ec}R_{ec}R_{ec}$ units previously supposed, we should consider if this structure is consistent with the STM images observed. The lower panels in Fig. 3 show a simulation of the STM images for the different structures. STM simulations of the $R_{ec}R_{ec}R_{ec}$ structure (I) are characterised by a rather uniform intensity distributed across the trimer, with poor differentiation between the separate bitartrate molecules. In contrast, the $R_{ec}O_aR_{ec}$ and $O_aR_{ec}O_a$ structures (II) and (III) both show well defined features associated with the individual bitartrate molecules and, importantly, a greater intensity on bitartrate molecules adsorbed with the O_a footprint rather than the R_{ec} configuration. Such an intensity alternation is also observed in the experimental STM images, Fig. 1a and b, and is consistent with the minimum energy $R_{ec}O_aR_{ec}$ arrangement, structure (II), but not with either the $R_{ec}R_{ec}R_{ec}$ or $O_aR_{ec}O_a$ structures. In fact the $R_{ec}O_aR_{ec}$ arrangement, structure (II), was the only structure we found that reproduced the STM images observed in experiment acceptably, confirming that the bitartrate phase is built from hydrogen-bonded trimers arranged with an $R_{ec}O_aR_{ec}$ footprint.

iii. Chiral segregation. The most important characteristic of the bitartrate/Cu(110) system is the segregation of a racemic mixture of (*R*,*R*) and (*S*,*S*) bitartrate into separate homochiral domains at the surface, with (*R*,*R*)-bitartrate forming (1 2, −9 0) domains while (*S*,*S*)-bitartrate separates into mirror (9 0, −1 2) domains, Fig. 1a. This experimental result implies that there is a clear energy advantage for an enantiomer to pack into one chiral domain, rather than its mirror assembly. We therefore investigated the binding energy of pure (*S*,*S*) and mixed (*R*,*R*)/(*S*,*S*) bitartrate structures accommodated within the (*R*,*R*) (1 2, −9 0) unit cell with the different footprint combinations shown in Table 1. The mixed (*R*,*R*)/(*S*,*S*) structures (VIII–X) were configured to allow H-bond formation between the units, to test if inter-molecular H bond formation can also stabilise mixed structures. The results for the originally proposed $R_{ec}R_{ec}R_{ec}$ arrangement (I) are particularly interesting. When *S*,*S*-bitartrate is accommodated within the (1 2, −9 0) $R_{ec}R_{ec}R_{ec}$ structure (V, Table 1), two internal H-bonds

break to form inter-molecular H-bonds between neighbouring OH groups and the (*S*,*S*) structure is actually slightly more stable than the *R*,*R*-bitartrate structure with the same footprint. This result would contradict the experimental observation that enantiopure *R*,*R*-bitartrate adopts the (1 2, −9 0) structure, while *S*,*S*-bitartrate prefers the mirror arrangement.[20,21] Similarly, when a mixture of (*R*,*R*)/(*S*,*S*) enantiomers are accommodated within the $R_{ec}R_{ec}R_{ec}$ arrangement (structure VIII) the energy is again slightly lower than that of the enantiopure (*R*,*R*) structure (I) in the same arrangement. The stability of (*S*,*S*) and mixed enantiomer structures based on R_{ec} units in the (1 2, −9 0) (*R*,*R*) unit cell (V and VIII relative to structure I) suggests that chiral segregation should not be observed for the racemic system, a prediction that clearly contradicts the experimental observation that the enantiomers separate into homochiral domains and implies the $R_{ec}R_{ec}R_{ec}$ arrangement cannot be correct. Turning to the $R_{ec}O_aR_{ec}$ footprint combination, we find that accommodation of three (*S*,*S*) units (structure VI) or a (*S*,*S*):(*R*,*R*):(*S*,*S*) combination (structure X) are 0.160 and 0.110 eV per molecule less stable than the enantiopure (*R*,*R*) structure II, respectively. Such energy penalties are sufficient to drive chiral segregation of the enantiomers into separate mirror domains at the temperatures studied. We note that in none of the enantiomer-footprint combinations we investigated were the inter-molecular hydrogen bonds formed as short as those of the pure *R*,*R* enantiomer accommodated in the $R_{ec}O_aR_{ec}$ footprint within the (1 2, −9 0) unit cell (structure II, Fig. 3b), suggesting that the formation of strong inter-molecular hydrogen bonds is the driving force behind the chiral separation of bitartrate that is observed on Cu(110).

iv. Modelling the gap. A key feature of the low coverage bitartrate structure is the formation of an exposed Cu channel between the bitartrate chains. Although long range dispersion interactions between the bitartrate trimers might explain formation of the extended chains, the presence of bare metal between them implies there must be an unfavourable Coulomb or through surface interaction preventing the chains from getting closer. To see if the $R_{ec}O_aR_{ec}$ trimer structure correctly reproduces this Cu channel we calculated the binding energy of this structure as a function of the separation between the chains. Fig. 4 shows the trimer assembly as the repeat distance of the unit cell is progressively elongated along the [1-10] direction, from 7 to 10 Cu atoms. We find that there is no significant change in the bitartrate geometry. The binding energy of the chiral assembly is a maximum for the (1 2, −9 0) unit cell observed experimentally, reducing by 0.016 eV per molecule as the chains are moved one unit closer together. Increasing the chain separation has no significant effect, consistent with the combination of long-range dispersion or through surface interactions and short range repulsion between the bitartrate keeping the chains just 3 Cu atoms apart. Inter-chain repulsion has been attributed to strain in the Cu close packed rows caused by a 2.5% expansion of the Cu–Cu distance in the atoms beneath the carboxylate ligands, preventing more than three bitartrate units bonding along adjacent Cu atoms.[23] This expansion is also observed in our calculations, (see ESI,† Table S1), with the R_{ec} footprint inducing a 2.6% expansion along ⟨1−10⟩, while the O_a and O_b footprints induce smaller distortions of the Cu surface. The need to relax strain between the Cu surface atoms also explains why addition of another molecule in the gap destabilises the structure (Table S4 and Fig. S8, ESI†), despite forming a strong H-bond to the bitartrate chain.

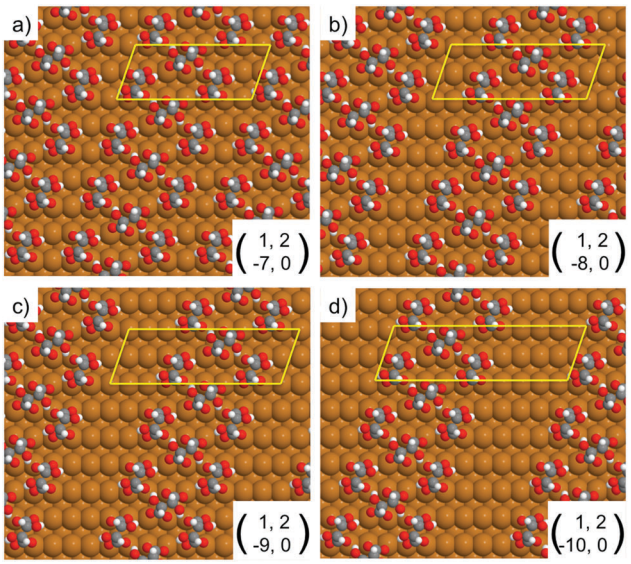

Fig. 4 Unit cells simulated by DFT for the $R_{ec}O_aR_{ec}$ chain structure showing the width of the exposed Cu channel as the unit cell is progressively elongated from 7 to 10 Cu atoms along the ⟨1−10⟩ direction. The local geometry of bitartrate in the trimer chains remains the same as in Fig. 3b.

4. Discussion and conclusions

Our results for bitartrate adsorption on Cu(110) indicate that bitartrate can adopt two different footprints on the surface, changing its molecular footprint from a rectangular to an oblique arrangement depending on its local adsorption environment. Bitartrate forms chains of trimers arranged in a staggered $R_{ec}O_aR_{ec}$ configuration, allowing the central O_a molecule to form strong hydrogen bonds to the neighbouring carboxylate groups and stabilising the homochiral phase. This result was unanticipated and changes our understanding of the driving forces that lead to chiral assembly and segregation in this system. The homochiral phase is more stable than mixed phases because it can form short strong H-bonds across the trimer, something that does not occur for mixed enantiomers. It is notable that, although bitartrate bonds to the surface *via* 4 strong O-metal bonds, the adsorption footprint is still able to respond dynamically to the presence of co-adsorbates to which it can form strong hydrogen bonds. Further work has shown that other polar species, such as water, can also cause bitartrate to restructure its adsorption footprint, implying that the chiral surface will be highly dynamic when other polar co-adsorbates are present. Such a dynamic local response has significant implications in systems where the bitartrate species acts as a chiral modifier during heterogeneous enantioselective catalysis,[3,4] for example in hydrogenation over tartaric acid modified RANEY® nickel catalysts. Although these systems show no long range order, experiments find enantioselective

reaction is accelerated by a direct hydrogen-bonding interaction between the bitartrate modifier and the substrate molecule,[48] implying a local ordering of the reaction complex. The results obtained here imply that models for chiral segregation and ordering, and for selective chiral catalysis using modifiers such as bitartrate, must account properly for the dynamic response of the enantiomer and its adsorption footprint to the local environment, which may lead to complex and sensitive responses as reactant and reaction conditions are altered.

Acknowledgements

This research was supported by UK EPSRC (EP/F00981X/1, EP/J019844/1, EP/K039687/1), EU 7th framework small scale collaborative project RESOLVE (NMP4-SL-2008-214340), EU Marie Curie Programs CHEXTAN (MRTN-CT-2004-512161) and Royal Society (IE131424). This work made use of the HECToR national high-performance computing service *via* our membership of the UK's HEC Materials Chemistry Consortium (EP/L000202 and EP/F067496).

References

1 L. Perez-Garcia and D. B. Amabilino, *Chem. Soc. Rev.*, 2007, **36**, 941–967.
2 H. Xu, W. J. Saletra, P. Iavicoli, B. Van Averbeke, E. Ghijsens, K. S. Mali, A. Schenning, D. Beljonne, R. Lazzaroni, D. B. Amabilino and S. De Feyter, *Angew. Chem., Int. Ed.*, 2012, **51**, 11981–11985.
3 V. Demers-Carpentier, G. Goubert, F. Masini, R. Lafleur-Lambert, Y. Dong, S. Lavoie, G. Mahieu, J. Boukouvalas, H. L. Gao, A. M. H. Rasmussen, L. Ferrighi, Y. X. Pan, B. Hammer and P. H. McBreen, *Science*, 2011, **334**, 776–780.
4 A. J. Gellman, W. T. Tysoe and F. Zaera, *Catal. Lett.*, 2015, **145**, 220–232.
5 V. K. Valev, J. J. Baumberg, C. Sibilia and T. Verbiest, *Adv. Mater.*, 2013, **25**, 2517–2534.
6 D. J. Dijken, J. M. Beierle, M. C. A. Stuart, W. Szymanski, W. R. Browne and B. L. Feringa, *Angew. Chem., Int. Ed.*, 2014, **53**, 5073–5077.
7 I. Dolamic, S. Knoppe, A. Dass and T. Burgi, *Nat. Commun.*, 2012, **3**, 798.
8 Y. W. C. Cao, R. C. Jin and C. A. Mirkin, *Science*, 2002, **297**, 1536–1540.
9 S. Katano, Y. Kim, H. Matsubara, T. Kitagawa and M. Kawai, *J. Am. Chem. Soc.*, 2007, **129**, 2511–2515.
10 P. Besenius, G. Portale, P. H. H. Bomans, H. M. Janssen, A. R. A. Palmans and E. W. Meijer, *Proc. Natl. Acad. Sci. U. S. A.*, 2010, **107**, 17888–17893.
11 N. Abdurakhmanova, A. Floris, T. C. Tseng, A. Comisso, S. Stepanow, A. De Vita and K. Kern, *Nat. Commun.*, 2012, **3**, 940.
12 A. Della Pia, M. Riello, A. Floris, D. Stassen, T. S. Jones, D. Bonifazi, A. De Vita and G. Costantini, *ACS Nano*, 2014, **8**, 12356–12364.
13 R. Otero, M. Lukas, R. E. A. Kelly, W. Xu, E. Laegsgaard, I. Stensgaard, L. N. Kantorovich and F. Besenbacher, *Science*, 2008, **319**, 312–315.
14 I. Temprano, G. Thomas, S. Haq, M. S. Dyer, E. G. Latter, G. R. Darling, P. Uvdal and R. Raval, *J. Chem. Phys.*, 2015, **142**, 101916.
15 P. Donovan, A. Robin, M. S. Dyer, M. Persson and R. Raval, *Chem. – Eur. J.*, 2010, **16**, 11641–11652.
16 M. Forster, M. S. Dyer, M. Persson and R. Raval, *J. Am. Chem. Soc.*, 2011, **133**, 15992–16000.
17 M. Forster, M. S. Dyer, M. Persson and R. Raval, *J. Am. Chem. Soc.*, 2009, **131**, 10173–10181.
18 R. B. Rankin and D. S. Sholl, *J. Phys. Chem. B*, 2005, **109**, 16764–16773.
19 M. Forster, M. S. Dyer, M. Persson and R. Raval, *Angew. Chem., Int. Ed.*, 2010, **49**, 2344–2348.
20 M. O. Lorenzo, C. J. Baddeley, C. Muryn and R. Raval, *Nature*, 2000, **404**, 376–379.
21 M. O. Lorenzo, S. Haq, T. Bertrams, P. Murray, R. Raval and C. J. Baddeley, *J. Phys. Chem. B*, 1999, **103**, 10661–10669.
22 L. Barbosa and P. Sautet, *J. Am. Chem. Soc.*, 2001, **123**, 6639–6648.
23 C. G. M. Hermse, A. P. van Bavel, A. P. J. Jansen, L. Barbosa, P. Sautet and R. A. van Santen, *J. Phys. Chem. B*, 2004, **108**, 11035–11043.
24 V. Humblot, M. O. Lorenzo, C. J. Baddeley, S. Haq and R. Raval, *J. Am. Chem. Soc.*, 2004, **126**, 6460–6469.
25 M. Parschau, S. Romer and K. H. Ernst, *J. Am. Chem. Soc.*, 2004, **126**, 15398–15399.
26 J. Zhang, T. Lu, C. Jiang, J. W. Zou, F. Q. Cao and Y. D. Chen, *J. Chem. Phys.*, 2009, **131**, 144703.
27 A. J. Gellman, *ACS Nano*, 2010, **4**, 5–10.
28 S. Y. Li, T. Chen, L. Wang, B. Sun, D. Wang and L. J. Wan, *Langmuir*, 2016, **32**, 6830–6835.
29 M. Mahapatra and W. T. Tysoe, *J. Phys. Chem. C*, 2016, **120**, 2309–2319.
30 R. Raval, *CATTECH*, 2001, **5**, 12–28.
31 T. Burgi and A. Baiker, *Acc. Chem. Res.*, 2004, **37**, 909–917.
32 A. Sanchez-Castillo, C. Noguez and I. L. Garzon, *J. Am. Chem. Soc.*, 2010, **132**, 1504–1505.
33 M. Forster, R. Raval, J. Carrasco, A. Michaelides and A. Hodgson, *Chem. Sci.*, 2012, **3**, 93.
34 S. Haq, N. Liu, V. Humblot, A. P. J. Jansen and R. Raval, *Nat. Chem.*, 2009, **1**, 409–414.
35 G. Kresse and J. Furthmuller, *Phys. Rev. B: Condens. Matter Mater. Phys.*, 1996, **54**, 11169–11186.
36 G. Kresse and J. Hafner, *Phys. Rev. B: Condens. Matter Mater. Phys.*, 1993, **47**, 558–561.
37 J. Klimes, D. R. Bowler and A. Michaelides, *J. Phys.: Condens. Matter*, 2010, **22**, 022201.
38 J. Klimes, D. R. Bowler and A. Michaelides, *Phys. Rev. B: Condens. Matter Mater. Phys.*, 2011, **83**, 195131.
39 P. E. Blöchl, *Phys. Rev. B: Condens. Matter Mater. Phys.*, 1994, **50**, 17953–17979.
40 G. Kresse and D. Joubert, *Phys. Rev. B: Condens. Matter Mater. Phys.*, 1999, **59**, 1758–1775.

41 J. Tersoff and D. R. Hamann, *Phys. Rev. Lett.*, 1983, **50**, 1998–2001.
42 N. Lorente and M. Persson, *Faraday Discuss.*, 2000, **117**, 277–290.
43 B. S. Mhatre, V. Pushkarev, B. Holsclaw, T. J. Lawton, E. C. H. Sykes and A. J. Gellman, *J. Phys. Chem. C*, 2013, **117**, 7577–7588.
44 T. J. Lawton, V. Pushkarev, D. Wei, F. R. Lucci, D. S. Sholl, A. J. Gellman and E. C. H. Sykes, *J. Phys. Chem. C*, 2013, **117**, 22290–22297.
45 K. H. Ernst, *Phys. Status Solidi B*, 2012, **249**, 2057–2088.
46 M. O. Lorenzo, V. Humblot, P. Murray, C. J. Baddeley, S. Haq and R. Raval, *J. Cat.*, 2002, **205**, 123–134.
47 N. Liu, S. Haq, G. R. Darling and R. Raval, *Angew. Chem., Int. Ed.*, 2007, **46**, 7613–7616.
48 T. Sugimura, S. Nakagawa, N. Kamata, T. Tei, T. Tajiri, R. Tsukiyama, T. Okuyama and Y. Okamoto, *Bull. Chem. Soc. Jpn.*, 2015, **88**, 271–276.